Tomographic reconstruction of the refractive index with hard X-rays: an efficient method based on the gradient vector-field approach

Sergei Gasilov,[1,*] Alberto Mittone,[1,2] Emmanuel Brun,[1,3] Alberto Bravin,[3], Susanne Grandl,[2] Alessandro Mirone,[3], and Paola Coan[1,2]

[1]*Department of Physics, Ludwig Maximilians University, Garching 85748, Germany*
[2]*Institute for Clinical Radiology, Ludwig-Maximilians-University, Munich 81377, Germany*
[3]*European Synchrotron Radiation Facility (ESRF), Grenoble 38043, France*

[*]*sergey.gasilov@kit.edu*

Abstract: The refractive-index gradient vector field approach establishes a connection between a tomographic data set of differential phase contrast images and the distribution of the partial spatial derivatives of the refractive index in an object. The reconstruction of the refractive index in a plane requires the integration of its gradient field. This work shows how this integration can be efficiently performed by converting the problem to the Poisson equation, which can be accurately solved even in the case of noisy and large datasets. The performance of the suggested method is discussed and demonstrated experimentally by computing the refractive index distribution in both a simple plastic phantom and a complex biological sample. The quality of the reconstruction is evaluated through the direct comparison with other commonly used methods. To this end, the refractive index is retrieved from the same data set using also (1) the filtered backprojection algorithm for gradient projections, and (2) the regularized phase-retrieval procedure. Results show that the gradient vector field approach combined with the developed integration technique provides a very accurate depiction of the sample internal structure. Contrary to the two other techniques, the considered method does not require a preliminary phase-retrieval and can be implemented with any advanced computer tomography algorithm. In this work, analyzer-based phase contrast images are used for demonstration. Results, however, are generally valid and can be applied for processing differential phase-contrast tomographic data sets obtained with other phase-contrast imaging techniques.

OCIS codes: (110.6955) Tomographic imaging; (110.7440) X-ray imaging; (120.5710) Refraction; (110.3010) Image reconstruction techniques.

References and links

1. A. Momose, "Demonstration of phase-contrast X-ray computed tomography using an X-ray interferometer," Nucl. Instr. Meth. Phys. Res. A **352**, 622–628 (1995).
2. V.A. Bushuev and A.A. Sergeev, "Inverse problem in the X-ray phase contrast method," Technical Phys. Lett. **25**, 83–85 (1999).

3. A. Maksimenko, M. Ando, S. Hiroshi, and T. Yausa, “Computed tomographic reconstruction based on x-ray refraction contrast,” Appl. Phys. Lett. **86**, 124105 (2005).
4. F. Pfeiffer, C. Kottler, O. Bunk, and C. Davis, “Hard X-Ray Phase Tomography with Low-Brilliance Sources,” Phys. Rev. Lett. **98**, 108105 (2007).
5. A. Bravin, P. Coan, and P. Suortti, “X-ray phase-contrast imaging: from pre-clinical applications towards clinics,” Phys. Med. Biol **58**, R1–R35 (2013).
6. F. A. Dilmanian, Z. Zhong, B. Ren, X. Y. Wu, L. D. Chapman, I. Orion, and W. C. Thomlinson, “Computed tomography of x-ray index of refraction using the diffraction enhanced imaging method,” Phys. Med. Biol. **45**, 933–946 (2000).
7. T. Weitkamp, A. Diaz, Ch. David, F. Pfeiffer, M. Stampanoni, P. Cloetens, and E. Ziegler, “X-ray phase imaging with a grating interferometer,” Opt. Express. **13**, 6296-6304 (2005).
8. P. R. T. Munro, L. Rigon, K. Ignatyev, F. C. M. Lopez, D. Dreissi, R.D. Speller, and A. Olivo, “A quantitative, non-interferometric X-ray phase contrast imaging techniques,” Opt. Express **21**, 647–661 (2012).
9. T. Yuasa, A. Maksimenko, E. Hashimoto, H. Sugiyama, K. Hyodo, T. Akatsuka, and M. Ando, “Hard-x-ray region tomographic reconstruction of the refractive-index gradient vector field: imaging principles and comparisons with diffraction-enhanced-imaging-based computed tomography,” Opt. Lett. **31**, 1818–1820 (2006).
10. M. N. Wernick, Y. Yang, I. Mondal, D. Chapman, M. Hasnah, Ch. Parham, E. Pisano, and Z. Zhong, “Computation of mass-density images from x-ray refraction-angle images,” Phys. Med. Biol. **51**, 1769-1778 (2006).
11. T. Thuering, P. Modregger, B. R. Pinzer, Z. Wang, and M. Stampanoni, “Non-linear regularized phase retrieval for unidirectional X-ray differential phase contrast radiography,” Opt. Express **19**, 25542–25558 (2011).
12. G. W. Faris and R. L. Byer, “Three-dimensional beam deflection optical tomography of a supersonic jet,” Appl. Opt. **27**, 5202–5212 (1988).
13. A. C. Kak and M. Slaney, *Principles of Computerized Tomographic Imaging* (IEEE Press, 1988, Chap. 5).
14. F. J. Harris “On the Use of Windows for Harmonic Analysis with the Discrete Fourier Transform,” Proc. IEEE, **66**, 51–83 (1978).
15. A. J. Devaney, “A Computer Simulation study of Diffraction Tomography,” IEEE Trans. Biomed. Eng. **30** 377–386 (1983).
16. A. Beck and M. Teboulle, “A fast Iterative Shrinkage-Thresholding Algorithm for Linear Inverse Problems,” SIAM J. Imaging Sciences **2**, 183–202 (2009).
17. R. P. Fedorenko, “A relaxation method for solving elliptic difference equations,” USSR Comput. Math. Math. Phys. **1**, 1092 (1961).
18. W. H. Press, S. A. Teukolsky, W. T. Vetterling, and B. P. Flannery, *Numerical recipes in C, 2nd edition* (Cambridge University, 1992, pp. 871–872).
19. J. M. Hyman and M. Shashkov ”Natural discretizations for the divergence, gradient, and curl on logically rectangular grids”, Computers Math. Applic. **33**, 81–104 (1997).
20. O. C. Zienkiewicz and K. Morgan, *Finite Elements and Approximation* (Dover Pubn. Inc., 2006, Chap. 3).
21. V. N. Ingal and E. A. Beliaevskaya, “X-ray plane-wave topography observation of the phase contrast from a non-crystalline object,” J. Phys. D **28**, 2314–2318 (1995).
22. A. Maksimenko, “Nonlinear extension of the X-ray diffraction enhanced imaging,” Appl. Phys. Lett. **90**, 154106 (2007).
23. Tissue Substitutes in Radiation Dosimetry and Measurement, ICRU Report 44 (1989).
24. G. R. Hammerstein, D. W. Miller, D. R. White, M. E. Masterson, H. Q. Woodard, and J. S. Laughlin, “Absorbed radiation dose in mammography,” Radiology **130**, 485–491 (1979).

1. Introduction

The application of X-ray phase contrast imaging (XPCI) for refractive index computed tomography (CT) was first investigated more than a decade ago [1, 2] and ever since it has continued to attract a vivid attention [3, 4]. As it was already discussed in the literature (see [5] and references therein), refraction-based CT may offer advantages over conventional X-ray tomography. XPCI methods have a very high sensitivity to fluctuations of the electron density and can be used for imaging of objects that exhibit almost no absorption-based contrast at high X-ray energies ($E > 50$ keV). By now several algorithms have been developed to extract refraction-contrast information from the XPCI measurements [6–8], allowing thus to perform refractive index CT in the hard X-ray spectral region. In general, the reconstruction procedure can be divided into three separate steps:

1. a CT data set of phase-contrast projections is recorded with a selected XPCI technique. The intensity in these images depends on both the attenuation and the refraction (i.e.

angular deflection) of the X-ray beam induced by the interaction with the sample. In this work we focus on the so-called "in plane" XPCI CT arrangement [9], in which the phase-contrast signal depends on the amount of the X-ray deflections in the CT reconstruction plane.

2. The deflection angles of the X-rays are calculated in the object exit plane according to the XPCI method employed in the first step. In the geometrical optics approximation the angular deflection at a point in the object exit plane is linearly proportional to the local spatial derivative of the wave phase. That is why projections of the deflection angle are also referred to as differential phase contrast images.

3. The index of refraction distribution inside the object is reconstructed from the calculated projections of the deflection angle.

The third step can be done using three different approaches, as it is shown in Fig. 1. One can begin the reconstruction by performing the phase-retrieval from projections of the deflection angle [10, 11] and then use a standard CT algorithm to reconstruct the refractive index decrement $\delta(\boldsymbol{r}_\perp)$ in the object ($\boldsymbol{r}_\perp$ indicates the Euclidian coordinates in a reconstruction plane). Refraction-based CT imaging without preliminary phase-retrieval can be also performed. In this case two other methods can be applied: (a) the filtered backprojection algorithm (FBP) for gradient projections [12] and (b) the refractive index gradient vector field method [3]. In the former case (a) the FBP-based algorithm allows to reconstruct fluctuations of the refractive index decrement in a single step. However, because the implementation is based on Fourier transforms, the performance of this method may decrease if a limited number of projections is available or if the signal of interest abruptly varies in the reconstruction plane. In the second method (b) the components of the refractive index gradient can be reconstructed with an arbitrary CT algorithm [3, 9], for instance an iterative one, which can outperform Fourier-transform-based algorithms. In order to complete the reconstruction using the approach (b), the integration of this 2D vectorial refractive index gradient field should be performed in the object slice. This crucial step determines the quality of the refractive index CT image. Most importantly, after integration the absolute values of $\delta(\boldsymbol{r}_\perp)$ is obtained (similarly to the case in which the phase-retrieval is first applied), rather than only the fluctuating component of the $\delta(\boldsymbol{r}_\perp)$ that is instead provided by FBP-algorithm for gradient projections.

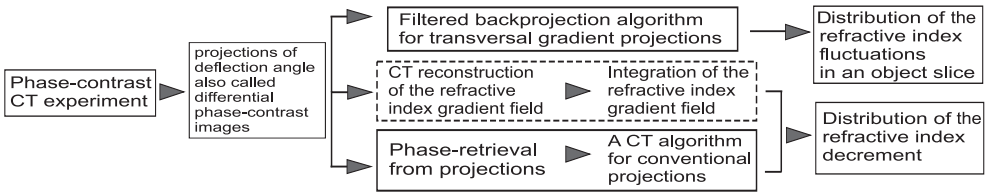

Fig. 1. A chart illustrating several possible ways to perform refractive index CT in the X-ray spectral range. The method adapted in this work is highlighted by the dashed line.

This work presents an approach that allows for an accurate CT reconstruction of the refractive index in bulky samples using a very moderate amount of projections. We have adapted the vectorial refractive index CT approach [3, 9] and suggest an efficient method for the integration of the refractive index gradient vector field. The method is applied to refraction-based CT imaging of a whole 75 mm thick human breast sample. It is shown that the combination of the vectorial approach with an iterative CT algorithm and the suggested integration technique

gives images with better spatial resolution and contrast compared to those obtainable with the FBP algorithm for gradient projections or images reconstructed through the phase-retrieval. While such a comparison can have a very high practical significance, to the best of our knowledge it has not been presented yet. The article is organized as follows: Section 1 shows how the reconstruction based on the vectorial approach can be completed by solving the Poisson equation and describes step-by-step the reconstruction recipe; in Section 2 we review the two other refractive index CT methods that were used for comparison; Section 3 describes the experimental set-up, the sample and the PCI technique used to obtain differential phase-contrast images in this work. Finally, the results of the refractive index CT reconstruction obtained with all the three considered methods are presented and their performance in terms of image quality is discussed.

2. Description of the suggested refraction-based CT method

We derive here the expression that relates the angular deflection of X-rays (a quantity which can be measured by means of an XPCI technique) to the distribution of the refractive index derivatives inside the object under investigation. The derivation begins with the common equation describing the paraxial propagation of the a scalar monochromatic X-ray wave in a media:

$$\frac{d}{ds}[n(\boldsymbol{r})\boldsymbol{t}(\boldsymbol{r})] = \nabla n(\boldsymbol{r}), \tag{1}$$

where s is an elementary interval along the ray; $\boldsymbol{r}$ is the spatial coordinate, $\boldsymbol{r} = \boldsymbol{r}(s)$ is the ray trajectory, $\boldsymbol{t}(\boldsymbol{r})$ is a unit vector tangential to the ray at the point $\boldsymbol{r}$, and $n(\boldsymbol{r})$ is the distribution of refractive index. Further we assume that: (1) the sensitivity plane of the XPCI method we use is defined as $x = const$, i.e. the phase-contrast signal does not depend on the amount of X-ray deflections out of the y-z plane (see Fig. 2); (2) the object rotation axis is perpendicular to the y-z plane (i.e. it corresponds to the x axis). The differentiation of Eq. (1) gives two relations:

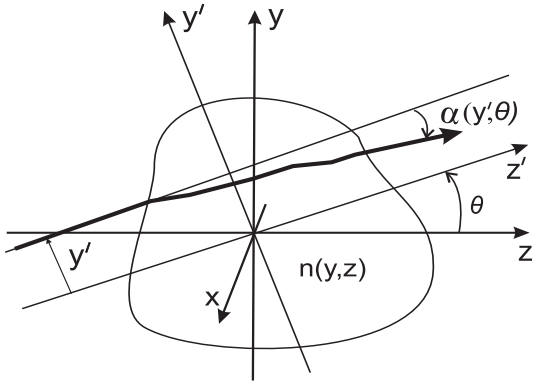

Fig. 2. Description of the coordinate systems used in the formalism.

$$\frac{dn}{ds} = \nabla n \cdot \boldsymbol{t}, \; \frac{d\alpha}{ds} = \nabla n \cdot \boldsymbol{v}, \tag{2}$$

where $\boldsymbol{v}$ is a unit vector normal to $\boldsymbol{t}$ and α is the angular deflection of an X-ray from the original propagation direction. Equations (2) can be integrated separately (see [9] for details). As a result

the following expressions for the components of the refractive index gradient vector field are obtained:

$$\begin{aligned} \alpha(y',\theta)sin\theta &= \int \frac{\partial n(y',z')}{\partial z'} dz'; \\ \alpha(y',\theta)cos\theta &= \int \frac{\partial n(y',z')}{\partial y'} dz', \end{aligned} \tag{3}$$

where the (y',z') axes are rotated by an angle θ with respect to the (y,z) axes, and ray trajectories are approximated as straight lines. Equations (3) are the main result of the vector field approach for refractive index CT [3, 9].

Projections of the deflection angle $\alpha(y')$ are characterized by sharp discontinuities arising at the interfaces between different features within the object. With respect to the absorption-based signal, these variations at the interfaces between different materials are more abrupt as in these regions refraction angles reach their local extrema. These sharp, spatially localized signal variations may significantly complicate the performance of the CT reconstruction [13]. Moreover, in many XPCI experiments the acquisition time and (or) the deposited dose are constraining factors (for instance in biomedical applications) and it might be necessary to limit the number of recorded projections. In these cases, the efficiency of FBP-based algorithms is reduced [13] and reconstruction artifacts may appear. For this reason it is important to utilize an efficient CT algorithm to solve Eqs. (3) in order to reconstruct the components of the refractive index partial derivatives. In this study we propose to use the technique named Dictionary Learning which has been recently implemented within our group. This reconstruction algorithm is an iterative method suited for non piecewise-constant images, which takes, as a-priori information, a set (that is called dictionary) of possible functions for small fragments of an image. The over-complete basis of these functions is generated using the algorithm proposed by Beck and Teboulle [16]. In the implementation that we have used, the dictionary was vectorial, i.e it had two entries, one for each component of the 2D gradient vector field of the refractive index. The reconstruction of both images is then made in parallel taking the advantage of the sparse representation of the signal that is related to the physical properties of the deflection angle projections discussed above.

Once the vector field of the refractive index gradient is obtained, the following problem must be solved in order to complete the reconstruction:

$$\nabla n = \boldsymbol{f}, \tag{4}$$

where the right-hand side vector $\boldsymbol{f} = (\partial n/\partial y, \partial n/\partial z)$ is the solution of Eq. (3). In practice, functions $\partial n/\partial y$ and $\partial n/\partial z$ and their first derivatives are non-smooth, particularly at the interfaces between an object and air. Moreover, because of the dose and (or) acquisition time constraints, the experimentally recorded images may have a very poor signal to noise ratio (for instance in the case of large and highly absorbing samples). Thus a direct integration of the Eq. (4) in the CT reconstruction plane can be very inefficient. We found that a robust and accurate way to solve Eq. (4) is to apply the divergence operator to its both sides. The divergence of the gradient is the Laplacian, thus Eq. (4) becomes:

$$\triangle n = div\boldsymbol{f}, \tag{5}$$

This is the Poisson equation that can be solved since the boundary condition of the first-type (Dirichlet) is known: $\delta(y,z)|_{(y,z)\in\Pi} = 0$, i.e. the decrement of the index of refraction δ ($n = 1-\delta$) is equal to zero at points outside the object, for instance, on the edges of a square Π bounding the reconstruction area in the *y*-*z* plane. The boundary conditions can be also defined for n as $n(y,z)|_{(y,z)\in\Pi} = 1$, i.e. the index of refraction of air outside the sample is set to one.

The resulting Dirichlet problem is a well-posed problem according to the classical definition. However, not any method is suitable to solve Eq. (5) because of the typically large size of XPCI images, which is determined by the use of high spatial resolution detectors with the pixel size of about 10-100 μm. For a centimeters-thick sample, the dimensions of the computational grid in the CT reconstruction plane can be very large. For instance, in the current work the integration was performed on a 765×765 pixels grid. To address this problem and to avoid using Fourier transforms, we applied a numerically stable and rapid approach to solve Eq. (5) based on a multigrid technique [17, 18]. The divergence operator in the right-hand side of the Eq. (5) was approximated as described in [19]. In case of samples with a slowly varying (with respect to the pixel size) quasihomogeneous distribution of the refractive index no additional regularization of Eq. (4) or smoothing of its right-hand side coefficients were necessary.

Summarizing the section, in order to perform the refractive-index CT reconstructions it is proposed: 1) to use the vectorial approach of Maksimenko *et. al* [3] for solving the X-rays propagation equation, 2) to reconstruct the 2D distributions of the refractive index gradient with the Dictionary Learning based CT algorithm (other high-performance CT algorithms can also be applied), 3) to obtain the spatial distribution of the refractive index by converting the integration problem to the Poisson equation. It is then suggested to use a multigrid technique to solve it.

3. Brief description of the alternative refractive-index CT reconstruction techniques

3.1. Filtered backprojection algorithm for gradient projections

As discussed in the introduction, a possible way to treat Eq. (1) is to perform its integration instead of the differentiation at the first step. This integration along the ray path gives the following approximate expression for the X-ray deflection angle in a plane $x = x_0$ through the object:

$$\alpha \approx \int \frac{\partial n(y,z)}{\partial y} dz, \tag{6}$$

which for the rotated coordinates shown in Fig. 2 becomes

$$\alpha(y',\theta) \approx \frac{\partial}{\partial y'} \int n(y',z') dz'. \tag{7}$$

According to the work by Faris and Bayer [12], who referred to the projection described by Eq. (7) as to the transverse gradient projection, the distribution of a given quantity inside an object can be found by making use of the Fourier transform derivative theorem:

$$\tilde{\delta}(y,z) = \int_0^{\pi} [\alpha(y',\theta) * g(y')]_{y'=-zsin\theta+ycos\theta} d\theta, \tag{8}$$

where $*$ denotes the convolution operator and the filter function, indicated with $g(y')$, is the inverse Fourier transform of the function $-\sqrt{-1}sgn(Y')/2\pi$; $sgn(Y')$ is the sign function in the reciprocal space. Equation (8) is the FBP algorithm for gradient projections. Note that instead of the index of refraction decrement, only its fluctuating component $\tilde{\delta}$ is recovered by Eq. (8). Although the difference operator in Eq. (3) removes the constant component of δ, this term can be recovered by taking into account an additional prior information about the boundary values [10].

According to the common estimation of the number of projections necessary for artifact-free reconstruction with FBP-based algorithm [13] about 1500 projections would be necessary for the size of the object that we imaged, while only 250 projections were used. To obtain the best

results from the algorithm Eq. (8) we employed a three-term Blackman-Harris window [14] when calculating Fourier transform of $\alpha(y')$. In this way, the ring artifacts and aliasing errors in the reconstructed images were efficiently suppressed [15].

3.2. The regularized phase-retrieval procedure

The third approach for refractive index CT is based on the phase-retrieval. The increment in the phase delay induced by an elementary volume of matter is linearly proportional to the value of the refractive index decrement in this volume: $d\phi(z) = k \cdot \delta(z)dz$, where k is the wavenumber. Thus, the total phase delay is related to δ through the ordinary Radon transform:

$$\phi(y', \theta) = k \cdot \int \delta(y', z')dz' \tag{9}$$

Comparing Eq. (9) to Eq. (7) (which relates the deflection angle to the Radon transform of the refractive index along the ray path), the phase spatial derivative at the object exit plane can be expressed as:

$$\frac{\partial \phi(x, y', \theta)}{\partial y'} = k\alpha(x, y', \theta), \tag{10}$$

where y' and θ are the tomographic coordinates as before and the coordinate along the axis of rotation x is indicated explicitly. In this case the idea of the phase-retrieval approach is to convert the deflection angles into the phase delays using Eq. (10). Refractive index projections defined by Eq. (9) are similar to the absorption ones as there is no differentiation operator as in Eq. (7). One can then use FBP algorithm with a standard ramp filter [13] or any other CT algorithm to reconstruct the refractive index in every point inside the object. In order to have comparable results we again used the Dictionary Learning iterative CT algorithm (see Section 2) in order to invert Eq. (9).

Despite its simple form, the integration of Eq. (10) poses a significant challenge: the inevitable presence of noise in the experimental data produces strong streaking artifacts along the integration direction (y'-axis). Frequently the phase projections obtained by direct integration could not be used neither to recognize fine object features nor for the tomographic reconstruction. In order to suppress the streaking artifacts Wernick *et al*. [10] and Tuering *et al*. [11] suggested to convert Eq. (10) to the constrained minimization problem. The constraint (i.e. a regularization term) is introduced to minimize variations of the phase in the direction perpendicular to the integration (x-axis in our notation). In the current work we used a slightly different approach to this problem. The initial value problem of Eq. (10) is converted to the boundary value problem by differentiating the left and right sides over y' once more:

$$\frac{\partial^2 \phi(x, y', \theta)}{\partial^2 y'} = k\frac{\partial \alpha(x, y', \theta)}{\partial y'}, \tag{11}$$

and afterward the regularization term is added to the left-hand side:

$$\frac{\partial^2 \phi(x, y', \theta)}{\partial^2 y'} + \gamma\frac{\partial^2 \phi(x, y', \theta)}{\partial^2 x} = k\frac{\partial \alpha(x, y', \theta)}{\partial y'}. \tag{12}$$

Just as in the case of the minimization approach [10, 11], Eq. (12) gives an approximate solution to the phase ϕ. The value of the regularization factor γ is chosen according to each particular case. It must be sufficiently large to suppress streaks, but not to large to avoid deviation of the approximate solution from the original function (to process the data acquired in the current work $\gamma = 0.05$ was used).

The finite elements method [20] was applied to solve the Eq. (12). This approach makes it possible not only to include boundary conditions, but also to easily utilize other a-priori

knowledge about the sample. For instance, we have taken into account the natural condition that the phase derivative must be very large at interfaces between an object and the air. We do not present here the detailed description of the phase-retrieval procedure because it is out of the scope of this paper. Another manuscript will be fully dedicated to this approach as it appears to be very efficient and particularly useful also for the index of refraction projection imaging.

4. Performance of the suggested method and comparison of the three techniques

Validation of reconstruction techniques was performed using the simple plastic phantom with known composition. In order to demonstrate the possible advantages of the considered approach we used the refraction-based CT to examine the internal composition of a whole human breast.

4.1. Acquisition of X-rays deflection angle projections

Experiments were performed at the biomedical beamline (ID17) of the European Synchrotron Radiation Facility (ESRF, France). The test phantom and the biomedical sample were both imaged under the same experimental conditions. The deflection angle projections were obtained by using the analyzer-based XPCI technique [3, 21]. A silicon crystal optics was used to produce a quasi-monochromatic ($\Delta E/E \sim 10^{-4}$), quasi-parallel X-ray beam. The photon energy was set to 52 keV. The XPCI signal was produced by means of a 3 cm thick and symmetrically cut perfect Bragg Si (333) crystal (the "analyzer") placed between the sample and the detector. The crystal rocking curve had a full width half maximum of about 1.8 μrad. The sample was rotated around the axis perpendicular to the plane containing the X-rays incident on and reflected from the analyzer crystal. A charge couple device detector with an effective pixel size of 96×96 μm^2 was used to register the images. The complete tomography data set consisted of 250 views (projections) uniformly sampling the range of $\theta = [0..\pi)$ rad. In such conditions two images at angular offsets of $\varphi_{1,2} \approx \pm 0.9$ μrad from the Bragg angle were obtained for every projection. The deflection angles were calculated using a non-linear extension for the diffraction enhanced imaging algorithm [22]. The obtained projections of the deflection angles were then used for the CT reconstruction of the refractive index with the adapted vectorial refractive index CT method, the FBP algorithm for gradient projections, and the phase-retrieval approach.

4.2. Testing of the reconstruction methods on a plastic phantom

The plastic phantom was composed of two coaxial cylinders. The inner polyethylene part with a diameter of 5.5 mm was embedded in the polymethylmethacrylate cylinder with an outer diameter of 14 mm. Density values were taken from the material supplier catalogue and the values for δ were calculated using the well-known electrodynamic equation $\delta = 2\pi\rho e^2/(m\omega^2)$ that relates material density ρ to the index of refraction decrement (e and m are the mass and the charge of the electron and ω is the X-ray wave frequency). The obtained values are ρ=0.93 g/cm^3, δ=8.60×10^{-8} and ρ=1.14 g/cm^3, δ=1.06×10^{-7} for the outer and the inner cylinder correspondingly.

Distributions of the material densities in a slice of the test phantom obtained using the described reconstruction methods are shown in Figs. 3(a)–3(d). The image in Fig. 3(d) is presented to illustrate the influence of experimental errors on the reconstruction quality. To obtain it, the FBP algorithm for gradient projections was applied to the analytically calculated projections of the deflection angles. Profiles in Fig. 3(e) show distributions of δ along the vertical line crossing the center of each image. Comparing the analytically obtained image (Fig. 3(d)) with the experimental data (Figs. 3(a)–3(c)) one can notice blurring at the edges of the sample and a slight asymmetry in both the images and corresponding profiles. The latter effect appeared due to the uncertainty in the angular position of the analyzer crystal. This systematic error was suppressed and did not influence results obtained for the breast sample.

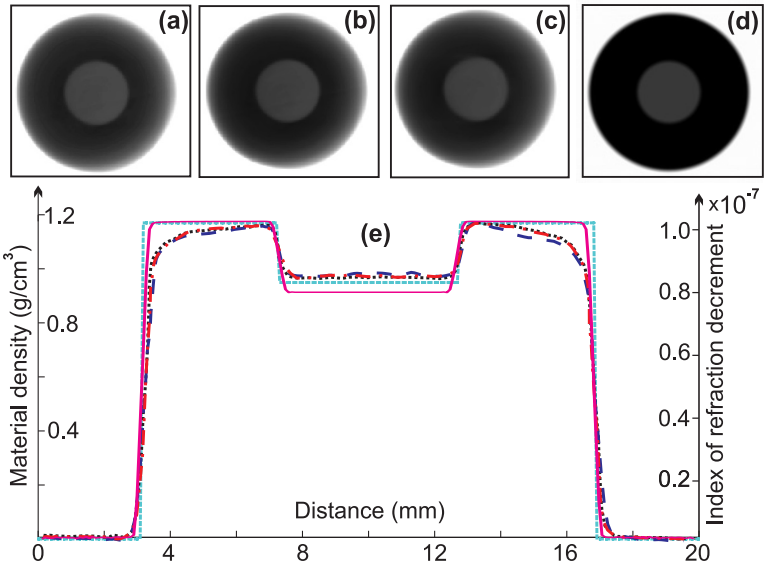

Fig. 3. Reconstruction of the materials density in the test phantom obtained with: (a) FBP algorithm for gradient projection, (b) presented method, (c) phase-retrieval based approach, and (d) FBP algorithm for gradient projection applied to the analytically calculated deflection angles. Panel (e) shows profiles of the material density taken along vertical line crossing the center of each image: case (a) is shown by the sparsely dashed blue line, (b) - black dotted line, (c) - dash-dotted red line, (d) - solid magenta line; cyan dashed line indicates the tabulated values.

The blurring at the interfaces between different materials is attributable to the detector blurring and noise. The discrepancy between the reconstructed results obtained from analytically calculated projections (Fig. 3(e) solid line) and the expected values (Fig. 3(e) cyan dashed line) is due to the inevitable discretization error in the finite difference scheme used for the calculation of the refraction angles. Analytically calculated values of the deflection angles are not affected by the properties of the real detector: for this reason the analytical profile exhibit much sharper transitions between different materials. The effect is most pronounced at the interface between the object and the air, where the δ experiences the largest variation: the typical values of the refraction angles there are one order of magnitude greater than everywhere inside the object and the measured phase-contrast signal is therefore greatly affected by the detector blurring. Correspondingly the reconstruction is spoiled near the outer sample border. None of the common deconvolution methods that we have tried was able to suppress this error without a global amplification of the high frequency noise. Nonetheless, it can be seen that the air interface blurring is rather localized and its effect is much less severe at the interfaces between materials inside the sample.

Apart from the analyzer crystal and the detector system, another source of systematic and statistical errors could be the in the X-ray beam fluctuations and instability. These errors are well suppressed by the periodic acquisition of the flat fields and proper normalization of the measured data, so that no evident effect can be noticed in the reconstruction. Summarizing the section we can note that in the case of the small sample with very simple structure, sufficient amount of projections acquired and ample exposure of the sample all three methods gave very similar result and quantitatively described the known properties of the sample. In the next

section it is shown that when a larger and more complex sample is examined (whose images generally have lower signal to noise ratio due to the higher absorption and the same number of projections is used for the CT reconstruction) each of algorithms demonstrates different reconstruction efficiency.

4.3. Imaging of a biomedical sample: results and discussion

The human breast sample was provided by the Department of Pathology of Ludwig Maximilians University of Munich, Germany. This formalin-fixed sample was embedded in a plexiglas container, with the wall thickness of 3 mm, so that the maximum projected thickness of the object was about 75 mm. Figure 4 presents the refractive index distribution in a slice of the breast sample reconstructed with two reference methods [Figs. 4(a) and 4(c)] and the suggested technique [Fig. 4(b)]. The skin, the adipose and glandular tissues, and the formalin can be easily distinguished in all three images. However, it can be readily seen that the image in Fig. 4(b) has the best sharpness, which allows observing finer density variations and structural alterations in different tissues within the breast. These fluctuations are correlated to real anatomical features as confirmed by the radiologist and by comparison with the histology results (this part of the analysis will be presented in another, medical-oriented work). The better delineation of the tissues in the image obtained with the suggested approach can be well seen in Figs. 4(f), 4(i), and 4(l), where the magnified region that contains soft tissues near the skin layer is shown (marked by dotted rectangles (2) in each slice). Strands of fat within the skin as well as fibrous strands in the fatty tissue are most accurately depicted in Fig. 4(i).

Figures 4(e), 4(h), and 4(k) show the region (marked by dotted rectangles (1) in the corresponding slices) in the sample containing a group of microcalcifications. Figure 4(h) allows noticing that there are possibly two microcalcifications next to each other.

The relative quality of the reconstruction was also evaluated using a simple statistical test. The distributions (histograms) of different tissues/materials versus their density have been calculated for each CT image. Conversion of the reconstructed quantity δ to the material density was done using standard tables that contain chemical composition of different biomedical materials [23, 24]. Distributions were generated using 255 bins for the density interval of 0.8–1.2 g/cm^3 and they were normalized on the total number of pixels in the image in order to show the relative amount of each material. For each image the absolute density values were computed by means of a multiplication by a normalization factor. Normalization factors for each image were estimated as the ratio between the reference formalin value and the average value of formalin computed in a 40×40 pixels region in the respective image. The reference value is the density of a 4% formalin solution ($\rho = 1.08$ g/cm^3, the corresponding peak can be seen in all three distributions). One can immediately notice that apart from the peak representing the formalin (almost the 45% of the slice consists of formalin) histograms in Figs. 4(g) and 4(j) have two distinct peaks that correspond to: (1) the adipose tissue, with $\rho \approx 0.96$ and $\rho \approx 0.95$ g/cm^3 for Figs. 4(b) and 4(c) respectively and (2) the small maximum at the density of ≈ 1.16 g/cm^3 in both images that represents the skin. The glandular tissue, whose expected density value is $\rho \approx 1.04$ g/cm, is not clearly distinguishable with respect to the other tissues/materials in any histograms (while it is very well recognizable in Fig. 4(b)).

According to these observations the suggested vectorial-based approach produces images that represent the internal structure of the sample better than the FBP-based algorithm and the phase-retrieval-based method. This result may be explained by the fact that neither smoothing (that causes the loss of image resolution and contrast) nor Fourier transforms are used in the computations with the suggested approach. However, it should be noticed that the smoothing caused by the regularization of the phase-retrieval problem can be useful for imaging of complicated inhomogeneous objects (for instance, joints) as it may suppress streaking artifacts arising

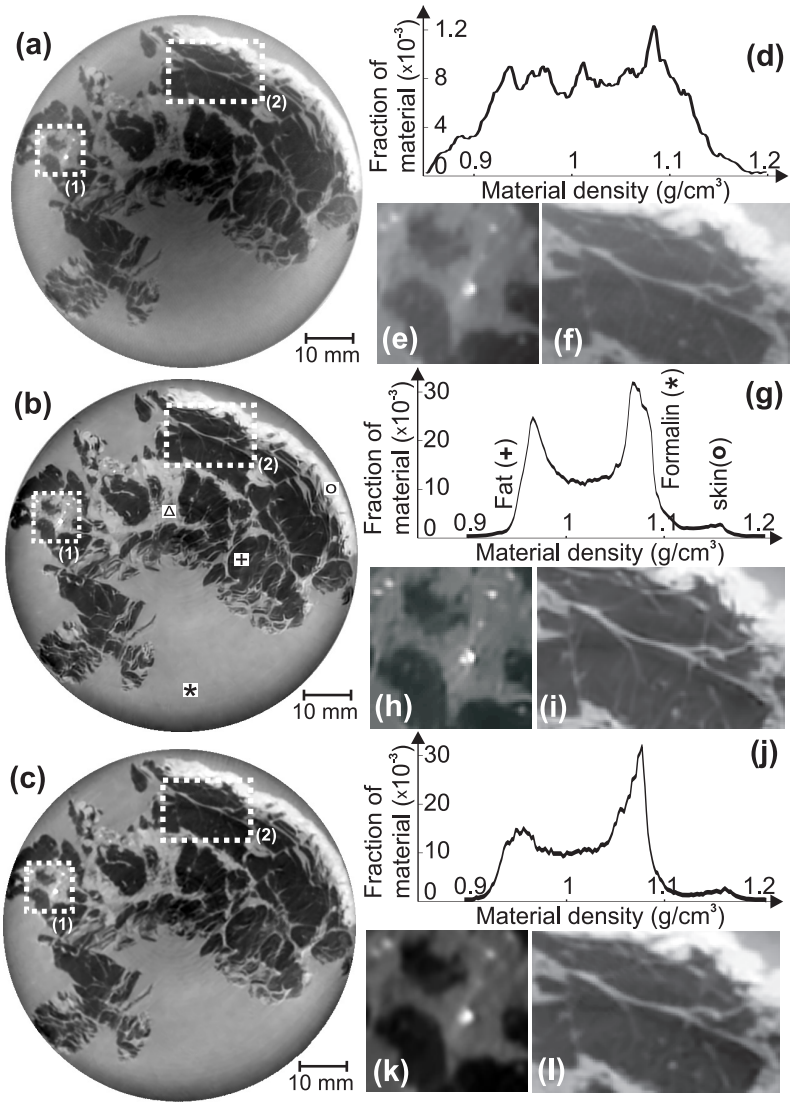

Fig. 4. Images of the refractive index decrement δ in a slice of a formalin-fixed human breast sample obtained using (a) FBP algorithm for gradient projections, (b) the adapted vectorial approach, and (c) by means of the phase-retrieval-based method. In all images the darker gray levels correspond to smaller values of δ (darkest parts are the adipose tissue, this area is indicated with the "$+$" sign in the panel (b)) and the brighter gray represents larger values of δ (almost white parts are the skin, indicated with the "*o*" sign in panel (b); the formalin and glandular tissues are correspondingly indicated with "$*$" and "$\triangle$" signs). Images (d), (g), and (j) represent the fraction of materials in the corresponding slices versus the material density derived from δ (number of bins is 255 for the density interval 0.8-1.2 g/cm^3). Insets (e), (h), and (k) show a group of microcalcifications (bright white spots) in the dotted rectangle (1) at the left side of the corresponding slices (note that there are possibly two closely spaced calcifications). A magnified region (marked by dotted rectangles (2) in each slice) that contains soft tissues is presented in panels (f), (i), and (l). Strands of fat within the skin as well as fibrous strands within the fatty tissue beneath are most accurately depicted in image (i).

at bone surfaces.

5. Conclusions

We considered the problem of the tomographic reconstruction of the index of refraction using data acquired with XPCI techniques. An efficient method for the integration of the refractive index gradient vector field is proposed. The gradient vector field approach and the suggested integration method were applied to a set of differential phase contrast projections of a whole human breast sample acquired with the analyzer-based imaging method and synchrotron X-rays. It is shown that obtained refractive index CT images can be used to distinguish between various anatomical features with high accuracy. The quality of the CT reconstructions was evaluated by a comparative study with two other methods: (1) the filtered backprojection algorithm for gradient projections and (2) the CT reconstruction from projections of the phase delays. It was found that these methods produced images with lower quality. This result can be partially explained with the fact that the considered approach does not require a preliminary phase-retrieval processing and it can be used in combination with iterative CT algorithms. If we compare images obtained with the phase-retrieval based method and the FBP algorithm for gradient projections, the former technique outperforms the latter in terms of overall image quality.

The combination of the vectorial approach with the suggested integration technique may find applications not only in the nondestructive testing and material science, but also in biomedical imaging as it produces index of refraction CT images of high quality even if a limited number of projections is available, thus allowing for a reduction of the acquisition time and of the dose deposited in the sample. The proposed method can be used to evaluate results of analyzer-based, grating interferometry, and coded aperture XPCI experiments.

Acknowledgments
Authors would like to acknowledge the financial support from Deutsche Forschungsgemeinschaft cluster of excellence - Munich Center for Advanced Photonics (EXE158) and the ESRF for provision of beamtime; H. Requardt, T. Brochard, C. Nemoz and the rest of the ID17 staff for the technical support at the beamline.